


## Instabilities and layering of a heated laboratory anticyclone

M. J. Burin <sup>1</sup>, J. Sommeria <sup>2</sup> and S. Viboud<sup>2</sup>

<sup>1</sup>*Department of Physics, California State University, San Marcos, San Marcos, California 92096, USA*

<sup>2</sup>*Univ. Grenoble Alpes, CNRS, Grenoble INP, LEGI, 38000 Grenoble, France*



(Received 2 August 2019; accepted 7 April 2020; published 2 June 2020)

We generate and observe large ( $\sim 1$  m diameter) anticyclonic vortices in a stably stratified rotating tank that are neutrally buoyant. A nonaxisymmetric ( $m = 2$ ) instability quickly develops, leading to subvortices and fine-structured shed filaments. When heated with respect to their surroundings the vortex lenses behave much the same way but with two conspicuous additions. First, prominent early, is that the circumferential edge appears serrated with cusplike features from lateral intrusions, surmised to be due to thermal convection. Second, a stepped upper layer develops due to thermohaline diffusive convection. We see no evidence of layering in the nonheated cases, indicating that viscohaline double diffusion appears to be inoperative, likely prevented by a turbulent background. These observations are considered with respect to previous laboratory work as well as to geophysical vortices that are thermally distinct from their environs, such as Meddies.

DOI: [10.1103/PhysRevFluids.5.063801](https://doi.org/10.1103/PhysRevFluids.5.063801)

### I. INTRODUCTION

In both the lab and natural settings, vortices represent a well-studied domain within fluid dynamics. A principal part of this subfield concerns vortex instability, which determines the lifetime of these coherent flows. How exactly instability leads to structural decoherence depends upon the initial distribution of vorticity along with other pertinent gradients. An ideal columnar vortex of uniform vorticity was shown to be linearly stable over a century ago [1], although more recent work has demonstrated nonlinear (or subcritical) instability at the vortex edge, yielding filamentation for finite vorticity gradients [2].

In the barotropic vortex experiments of [3], an  $m = 2$  instability, where  $m$  represents the azimuthal mode number, was usually seen to dominate the dynamical evolution. Initially monopolar cyclonic vortices yielded a tripolar structure (i.e., central elliptical cyclone with opposing satellite anticyclones), while anticyclonic vortices yielded a more dipolar structure, with its central core apparently gone, or at least much diminished. The anticyclonic instability was observed to be explosive and likely due to centrifugal instability, which can be explained with Rayleigh's circulation theorem extended to incorporate a (counter) rotating background. Considering the inflection point at the vortex edge, a concomitant shear instability cannot be ruled out, however. A review of earlier barotropic vortex experiments may be found in [4].

There have been a few vortex instability laboratory experiments to date with rotating stratified backgrounds, starting with Saunders [5], who demonstrated baroclinic instability of a circular vortex within a two-layer stably stratified fluid. Building off this work Griffiths and Linden [6] investigated vortex instabilities in a similar environment and found that the mode of the instability could be determined from the initial relative depth  $z_0/H$  (where  $z_0$  is the depth of an introduced cylindrical volume of fluid of differing density and  $H$  is the depth of the entire working volume), and a normalized Rossby radius of deformation,  $\theta_0 = g'z_0/f^2R_0^2$ , where  $g'$  is the reduced gravity  $g(\Delta\rho/\rho)$ ,  $f = 2\Omega$  is the Coriolis parameter, and  $R_0$  is the vessel radius. We note that  $\theta_0$  was introduced as a form of Richardson number, but might be more immediately seen as a form of Burger number in comparing the relative strength of buoyancy to rotation.

The relative depth  $z_0/H$  in [6] determined which instability energy source was favored (if  $z_0/H > 0.1$  and  $\theta_0 \ll 1$  then it was from flow potential; otherwise, shear), and it also determined what fraction of the central core was intact after satellite separation.  $\theta_0$  was correlated with the mode number:  $m = 2$  being dominant for  $\theta_0 > 10^{-1}$ , but with  $m = 3, 4,$  and  $5$  being observed for  $10^{-1} > \theta_0 > 10^{-2}$ . Stability was observed for  $\theta_0 > 1.8$ . Experiments with a continuous density gradient were also performed, with generally similar results, except that only  $m = 2$  was observed. More recent two-layer vortex experiments [7] have shown quantitative agreement of the instability growth rate with a quasigeostrophic model of baroclinic instability.

Homogenous injections into a continuous, linear density gradient were the experimental focus of Hedstrom and Armi [8], who recast the instability criterion in terms of  $N/f$  (as an alternate measure comparing buoyancy to rotation, where the buoyancy frequency  $N = \sqrt{-g\partial\rho(z)/\rho_0\partial z}$  and Rossby number  $Ro = \Omega_0/f$ , where  $\Omega_0$  is the angular frequency of the lens core).  $N/f$  was shown to be inversely proportional to the vortex aspect ratio  $\alpha = h/L$ , as predicted by analytic theory [9], which also predicted the decay of  $Ro$  and  $\alpha$  over time. The range of vortices observed spanned  $0.18 < N/f < 1.25$ , with higher values appearing less stable. Lens eccentricity was seen to be periodically minimized through the shedding of slower moving periphery into filaments, a primary-axis process for the elliptical lenses resembling the  $m = 2$  instability described above. More recent experiments with a continuous gradient were performed by Facchini and Le Bars [10], who observed the stable, slow spin-down of embedded anticyclones in the range  $0.41 < N/f < 0.75$  in a process well described by viscous diffusion.

In both [6] and [8] perturbed density layers were observed above and below the vortex lens in the presence of continuous stratification. These layers have been attributed to viscohaline double-diffusive instability [11], a class of instabilities owing to the differing rates of diffusion of two properties within a fluid (here salt and momentum). Initial experiments on this instability using a counter-rotating solid disk within a rotating stratified tank were first performed by Baker [12]. Further experiments by Calman [13], also with an embedded disk, traced the stability curve given in terms of a critical Richardson number  $Ri_c = (\sigma + 1)^2/4\sigma$ , where  $Ri = N^2/(dU/dz)^2$ , which reduces for typical saltwater ( $\sigma \gg 1$ ) to  $\sigma/4$  or about  $Ri_c = 175$ . The layer wavelength was found to be largely independent of  $Ri$  and equal to  $2\pi(\nu/f)^{1/2}$ , where  $\nu$  is the kinematic viscosity.

The oceanic significance of double diffusion, where typically heat and salt are the diffusing agents, was realized by Stommel *et al.* [14]. Beyond the seas, double-diffusive processes are now widely recognized to have applications from industrial metallurgy to stellar interiors [15]. While salt fingers are perhaps the most recognized manifestation of thermohaline double diffusion, diffusive layering and “staircase” structures may also result from double-diffusive convection (DDC, or semiconvection). This occurs, for example, when cool fresh water overlays warmer but saltier and denser water, as can be found within some geothermal lakes, as well as in polar regions having undercurrents of lower latitude origin [16]. Laboratory experiments featuring DDC now span over a half-century, using both heat/salt and the analogous sugar/salt pairing, starting with the pioneering experimental work of Turner [17]. Considerable uncertainty still exists regarding the dynamics of the layering process and with related flux laws, though there has been theoretical progress in recent years, e.g., by including minor shear [18].

Intermittent observations of mesoscale oceanic vortices have provided information for, and have been suggestive of, various instability candidates likely related to the discussion above. Conspicuous features include layering [19], lateral intrusions [20], and the occasional presence of spiral arms [21], the latter bearing some similarity to the  $m = 2$  instability seen in experiments. Ruddick [22] analyzed laterally coherent intrusions into the Meddy “Sharon” and concluded that they were likely due to thermohaline double diffusion, a hypothesis that was recently bolstered by numerical simulations [23].

While a handful of both finite-layer and continuously stratified experiments since [17] have observed thermohaline diffusive layering, none have apparently done so within a rotating background that would be relevant to planetary flows. On the other hand, vortex experiments to date within a rotating, stratified background have not explored thermal gradient effects. Our motivation then has

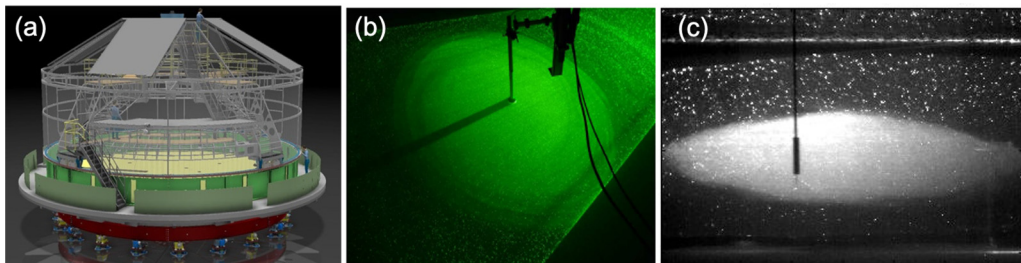


FIG. 1. Schematic of the 13 m diameter Coriolis II rotating platform (a) along with a top view (b) and side view [(c), seen 20 s after injection] of a typical anticyclonic vortex lens approximately 1.3 m in diameter. The vertical shaft affixes a plunging conductivity/temperature probe, which may be seen in the foreground.

been to perform initial laboratory experiments that explore thermohaline vortex decay in the hopes of forming a potential bridge between previous (isothermal) vortex laboratory experiments, previous (nonrotating) double-diffusion experiments, and geophysical data.

## II. APPARATUS AND DIAGNOSTICS

Experiments were performed on the Coriolis platform in Grenoble [see Fig. 1(a)], which has a working diameter of 13 m [24]. We used water with a stationary fluid depth of approximately 80 cm with the volume linearly stratified at 1%: it varied from 1.012 g/cc on bottom to nearly unity (1.002 g/cc) on top, yielding a buoyancy frequency  $N = 0.35$  rad/s. A small outflow pipe fixed at mid-depth allowed for volumes of fluid to be inserted. The pipe was orientated with the axis of rotation and was joined with the plane of two stacked disks 10 cm in diameter, separated by 1 cm, which allowed fluid to exit at all angles equally between the disks in the plane of rotation. The fluid influx was density matched to mid-depth with an accuracy of a few percent. Background rotation was maintained with a period of 80 s (angular frequency  $\Omega = 0.0785$  rad/s) with  $<0.1\%$  accuracy. For example vortices in Coriolis under similar conditions please see Fig. 1.

The inserted volumes, injected so as to have no initial absolute vorticity, take on anticyclonic vorticity with magnitude  $f$  in the rotating frame of reference, such that the theoretical initial Rossby number  $Ro = -\Omega/f = -1/2$ . However, turbulent mixing produced during injection leads to a dilution with the surrounding fluid, approximately doubling the lens volume, so that the resulting  $Ro$  magnitude is closer to half of this value. Earlier experiments [8,10] have shown a similar reduction in the initial  $Ro$  to near 0.3. The aspect ratio seen in Fig. 1(c) is  $\alpha \cong 1/4$ , a value that is a bit larger than is typical for our occasional observations of this quantity, which range from about 0.15 to almost 0.3, a variation that is discussed further below.

Besides simple imaging using fluorescent dye (rhodamine 6G), for diagnostics we used a combined 3D-PIV/LIF system (housed in the rotating frame of reference; for details see [25]). A continuous 6 W YAG green laser was used (wavelength 532 nm), equipped with an oscillating mirror to produce a horizontal laser sheet. The laser sheet was translated vertically from  $z = 15.2$  cm to  $z = 53.2$  cm, during which time 36 images were taken to scan a volume. Two such scans were taken with a time interval 1.44 s, to provide PIV by image correlation at each level. A longer time interval (15 s) was left between two successive volume pairs, considering the relatively slow evolution of the vortices. For PIV the flow was seeded with plastic particles (diameter 300  $\mu\text{m}$ ) matched in density with the local fluid.

The images were processed in two ways to get both velocity fields by PIV and dye concentration by LIF. For the latter the particles were removed from the images by taking the local image minima in small pixel blocks. The edge of the dyed fluid volume was initially fairly sharp, allowing the contour of the lens to be obtained using horizontal and vertical slices along with simple edge detection. We then fit this contour as a three axis ellipsoid to monitor the eddy volume.

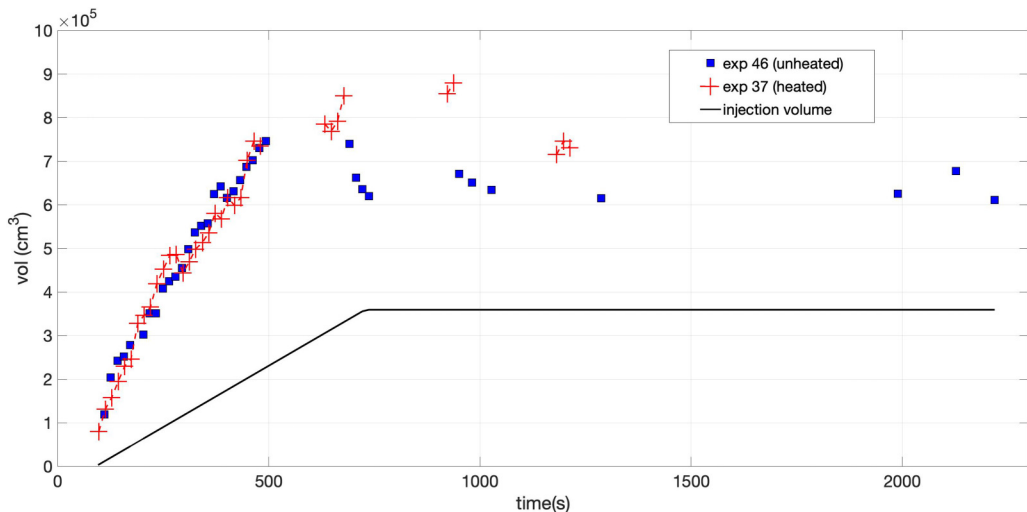


FIG. 2. LIF data comparing example heated (experiment 37) and unheated (experiment 46) cases with respect to volume. The black line indicates the influx volume, which remains constant after 750 s. The resulting vortex volumes show significant entrainment. Although data is sparse, more mixing may be inferred in the heated case.

Unfortunately, PIV data were mostly of poor quality because of weak luminosity and optical perturbations due to refraction effects. It was possible, however, to get representative PIV from one case, as shown below.

Imaging techniques were complemented by a plunging temperature/conductivity probe (MSCTI-125 by Precision Measurement Engineering, Inc.) that was vertically mounted to traverse depth. The traverse ranged 70 cm, from near the bottom of the tank ( $z = 0$ ) at a speed of 0.58 cm/s. Probe signals were calibrated using water of varying salt (NaCl) concentrations, allowing for density to be assessed at any temperature. Sensors were kept immersed during the entire run due to their sensitivity with drying. Sensor drift, stated by the manufacturer to be up to a 2–3% per day, was insignificant.

The flow rate to insert the vortex volumes for all experiments presented here is roughly 35 L/min, accurate to about 10%. We investigated three basic volumes, designated as small (30–35 L), medium (124–140 L), and large (360 L). Each size was repeated 2–3 times, at least once with heating ( $\Delta T \sim 5^\circ\text{C}$ , applied in a separate tank before intrusion) and once without. Like their mesoscale counterparts, the eddies usually wandered considerably during the course of each realization. Consequently, our examples are not equally represented in terms of useable data, and mainly the largest eddies are discussed below. Given the large diameter of the Coriolis vessel, combined with the relatively long lifetimes of the vortices ( $\leq 1$  day), only a handful of examples could be obtained within the period of experimentation.

### III. OBSERVATIONS AND DISCUSSION

The inserted fluid volumes become coherent anticyclonic vortices before the injection fully ceases, with eddy interiors being well mixed from the earliest stages of development. LIF data comparing heated and unheated cases is given in Fig. 2. The fluorescent dye was observed to be well mixed inside the vortex, with an initially sharp boundary, allowing a good measurement of the volume by edge detection, as explained above. From this data it appears that the amount of entrainment of surrounding fluid is about 50–120% more than the intrusion volume. During the injection time the volume initially increases similarly for both heated and unheated cases, with initial

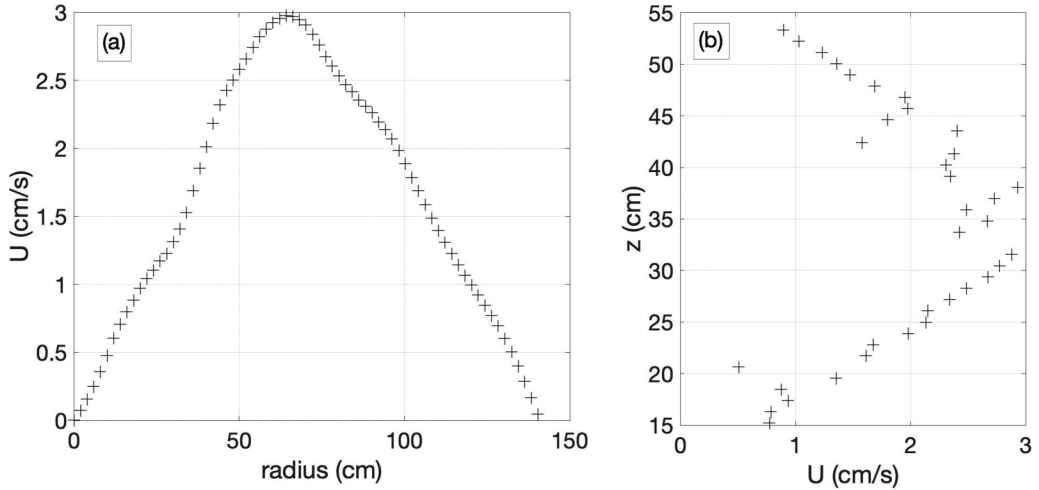


FIG. 3. Representative PIV profiles of the azimuthal velocity across the eddy shortly after the injection ceases,  $t = 771$  s (experiment 37, injection volume 360 L). Panel (a) is a horizontal cut at the vortex center ( $z = 37$  cm) and (b) is a vertical cut at the radius of maximum velocity ( $r = 65$  cm).

turbulence maintained by the injection source. By contrast, subsequent turbulence is maintained by convection for the heated case only, which explains the stronger entrainment and resulting higher volume. Other observations (both visual and probe) indicate that heated vortices are indeed more turbulent, and of greater vertical extent, consistent with this increased mixing.

Velocity profiles across a typical eddy in both the horizontal and vertical directions are shown in Fig. 3 for a time shortly after injection. From these plots we can deduce that the initial vorticity in  $z$  is  $\cong -0.08 \text{ s}^{-1}$  and that the vertical shear  $dU/dz \cong 0.17 \text{ s}^{-1}$ . While these profiles are for a heated example (experiment 37), they are thought to be adequately representative of unheated cases as well. The profiles in Fig. 3 also reveal a maximum azimuthal velocity  $U_{\max}$  near 3 cm/s at a radius of 65 cm, yielding  $\Omega_0 = -0.046 \text{ s}^{-1}$  and a nominal rotation period  $T$  near 140 s. This confirms a 40% spin down due to initial mixing with ambient fluid. We note that the profiles appear more piecewise linear than Gaussian, but until additional data can be obtained defer any discussion of their exact form.

We now consider the background stability of the vortices without regard to thermal effects. With the absence of significant waves, free surface effects are considered to be relatively unimportant, as are effects from the bottom boundary of the tank. Using the shear derived from Fig. 3(b) we may estimate  $\text{Ri} \approx 4$ . The lens is thus stable to shear, at least in the usual sense. We may also estimate the Burger number  $\text{Bu} = \alpha^2(N^2/f^2)$ . Using a representative aspect ratio of  $\alpha = 0.2$ , we find  $\text{Bu} = 0.2$ . Following recent analysis [26,27] for small Rossby number ( $|\text{Ro}| < 2$ ) and also small  $\text{Bu}$  ( $0.1 < \text{Bu} < 1$  in [27] and  $\text{Bu} < 0.45$  from [26]), we may identify the primary instability as a mixed baroclinic-shear mode. Further, it may be expected to be manifest as  $m = 2$  [27]. According to [26] baroclinic instability develops only for  $F_h/\alpha|1 + 1/\text{Ro}| \geq 1.46$ , where  $F_h = \Omega_0/N$  is the Froude number, and for our data we find this condition not to be met. However, this breaks down near  $\text{Ro} = -0.5$ , and in assuming  $d\Omega/dz \ll \Omega_{\max} + f/2$  along with (as with other analyses) the assumption of Gaussian profiles. Considering these caveats, it may well be that the observed instability is purely baroclinic. In any case, at  $\text{Ri} \approx 4$  we are also well within the instability criterion given for viscohaline double-diffusive instability, as discussed above. (That we do not observe it is discussed below.) Thus at least two different instabilities may be expected apart from thermal effects.

Sample images of the vortices shortly after inception are given in Fig. 4 for both heated and unheated cases. Besides a more turbulent inception, the heated vortices experience an additional instability, with its circumference appearing ringed with cusps at early times [i.e., for  $t \ll T$ ,



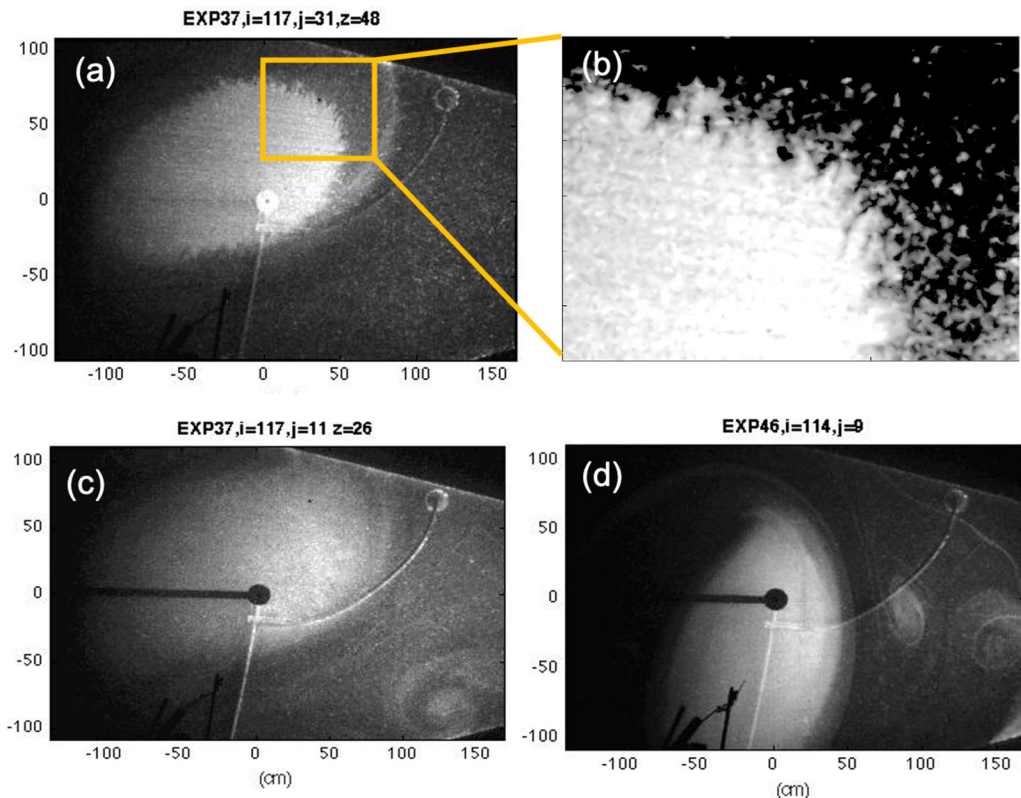


FIG. 4. Top view of vortices early in their evolution. The edge of the heated vortex appears serrated at higher  $z$  (a) with convective cusps on the scale  $\sim 3\text{--}5$  cm [closeup (b)]. At lower  $z$  (c), and for the unheated case at all  $z$  [e.g. (d)], the circumference appears relatively smooth. Note in (c) and (d) the presence of background satellite vortices, shed from earlier episodes of  $m = 2$  instability.

see Figs. 4(a) and 4(b)]. These cusps have a wavelength of 3–5 cm. This transient behavior is somewhat localized in depth to the upper part of the vortex, so that simultaneously a horizontal cross section at lower  $z$  appears smooth [Fig. 4(c)]. Visual observations of upslope billowing during this phase corroborate this picture. For comparison a representative unheated vortex slice is also given [Fig. 4(d)], revealing an unperturbed perimeter that is representative of all  $z$ .

As with [8], we find that filamentation, shed from the slower long-axis periphery (i.e.,  $m = 2$ ), leads to a periodic axisymmetrization of the lenses. Shed material often organizes into satellite vortices, as may be seen in the background in Fig. 4. Sinuous filaments that do not so organize also contribute to filling the domain. In Fig. 5 we present a cross-sectional view of a typical  $m = 2$  shedding event occurring over about 6 min. This particular example is heated, but the unheated case is similar in this respect. The development of a distinct fissure occurs in the first minute (40 s), while minutes later the peripheral material is more clearly separated. The material loss effectively reduces the lens radius, and thereby its moment of inertia. Subsequently it is observed to experience a slight spin-up. Also, its aspect ratio is somewhat increased, at least temporarily, until the next instability cycle starts.

The difference between heated and unheated cases is also significant later in their respective lifetimes, as seen in Fig. 6. This is primarily due to a few cm diffuse layer that forms above the heated vortex (see arrow). We see no evidence of layering in the nonheated cases, indicating that the role of viscohaline double diffusion appears to be inoperative for the unheated case. As discussed earlier, our relatively low  $Ri$  suggests otherwise, and the expected wavelength of  $2\pi(\nu/f)^{1/2} = 1.6$  cm

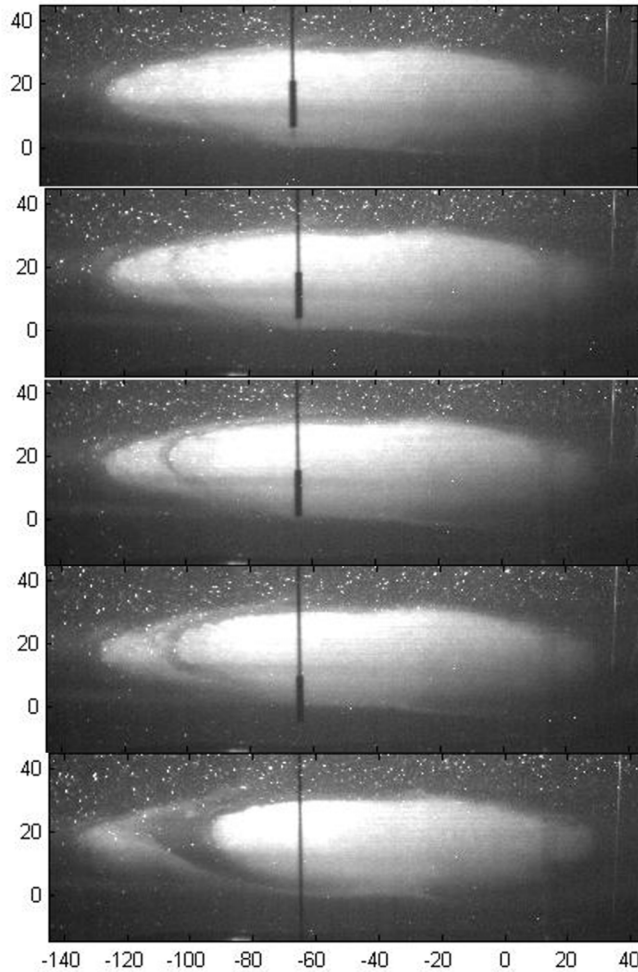


FIG. 5. Cross section of a typical  $m = 2$  shedding event, with time increasing for frames going downward. The development of a distinct fissure occurs in about 40 s (top three panels), while minutes later the peripheral material is more clearly separated. Scale is in cm.

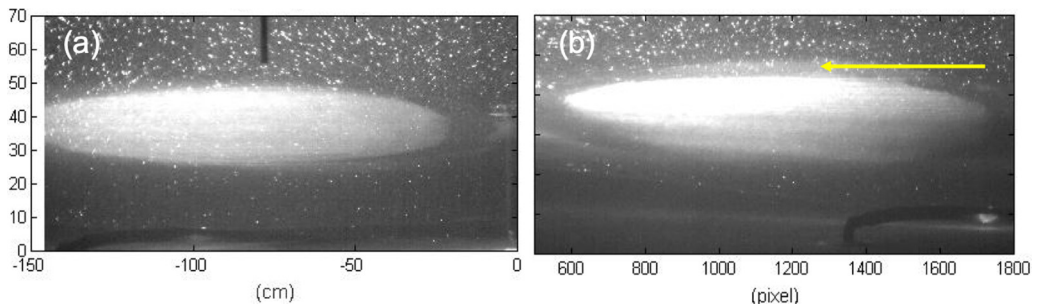


FIG. 6. Representative side view images of the vortices at intermediate times. A heated vortex lens (b) shows a diffuse layer that is a few cm thick directly above it (see arrow), which the unheated case (a) lacks. Note that the images do not necessarily show the entire vortex cross section as they are not exactly nor equally centered in the vertical laser sheet.

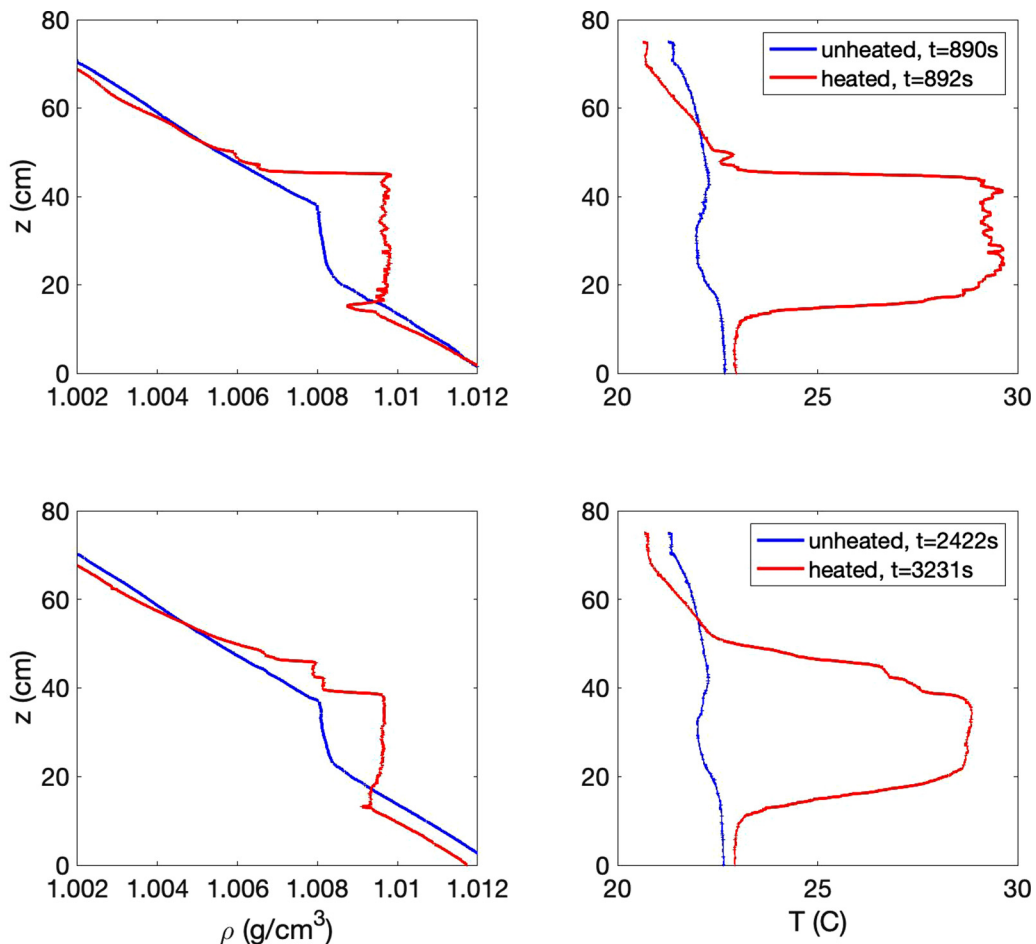


FIG. 7. Probe traces of density and temperature comparing earlier and later times for the unheated (blue) vs heated (red) cases. As the heated lens evolves, the rms decreases while a staircase pattern in density is seen to emerge near  $z = 40\text{--}45$  cm.

is well within probe resolution. We surmise that these layers are not seen due to the turbulent environment in and near the eddy. It is perhaps notable that viscohaline layering was first seen with a solid disk preexisting within (and thus not disturbing) the background stratified fluid, and the layers observed with a fluid intrusion [8] were observed after a relatively low filling rate (5–8 mL/s), which is two orders of magnitude less than ours (580 mL/s). Furthermore, while our initial intrusion was clearly turbulent, Ref. [8] utilized an aquarium air stone, further promoting laminarity.

More detail on the thermohaline layering seen with the heated case may be observed in the probe data given in Fig. 7, which contrasts temperature and density profiles for relatively early (890–892 s, with injection ending for these cases at 620 s) and later times ( $\sim 2400\text{--}3200$  s). The temperature of the unheated influx, seen between  $z = 20$  and 40 cm ( $h = 20$  cm), is a fraction of a degree cooler than expected, with the decay of earlier heated vortices having warmed the background a bit, but the overall profile is basically constant with  $z$ . It varies by about 1.5 C over the full depth, increasing slightly towards the bottom. The corresponding density profiles are observed to possess a smooth, finite gradient of approximately  $1.66 \times 10^{-5} \text{ gm/cm}^4$ . The transition region (i.e., vortex thickness,  $h$ ) is somewhat diminished over the time period observed, but this small decrease might be from off-centering due to lens lateral movement.



Besides an increase in temperature, the same intrusion volume, when heated, results in a slightly thicker lens, with  $h = 30$  cm, as is expected from increased turbulent mixing (Fig. 2). Both the initial temperature and density profiles lack a mean gradient and clearly show higher variance, also indicative of significant mixing. As the heated vortex evolves, the rms decreases while a staircase pattern in density is seen to emerge.

More detail on the heated case may be seen in Fig. 8, which provides temperature and density profiles for additional and later times. Besides the aforementioned rms decay, the average core temperature also gradually decays, going from 29.5 to 25.5 C over  $\Delta t = 7560$  s ( $\sim 2$  h). Concomitantly some larger scale variation develops, on the scale of a few cm: i.e., larger than the initial convective rms scale, similar to the convective cusp scale, and smaller than the vortex thickness  $h$ . This coarser variation in temperature was not equally present in every probe plunge, however, leading us to suspect that there may be significant lateral differences.

The density profiles in Fig. 8 show the beginning of staircase formation due to thermohaline diffusive convection. The first distinct step may be seen for  $t \geq 10^3$  s and a second distinct step may be discerned some 2000 s later; a third is not observed, up to  $t = 8180$  s (or about 60 T). This layering may be understood given the (inverse) diffusive density ratio

$$R_\rho^* = \frac{\beta}{\alpha_T} \frac{\frac{\partial S}{\partial z}}{\frac{\partial T}{\partial z}}, \quad (1)$$

where  $\beta$  is the coefficient of saline contraction,  $\alpha_T$  is the coefficient of thermal expansion, and the gradients of salinity ( $S$ ) and temperature are with respect to depth. This ratio may be approximated for finite  $\Delta z$  as  $\approx \frac{\beta}{\alpha_T} \frac{\Delta S}{\Delta T}$ , yielding  $R_\rho^* \approx 5$ . While doubly diffusive fluids are susceptible to diffusive layering for  $0 < R_\rho^* < \infty$ , it is typically observed at  $R_\rho^* < 10$  [16].

Step heights are approximately 2 cm. Following the basic scaling analysis found in Radko [15], where buoyancy, viscous dissipation, and pressure gradients are assumed to be of the same order, the primary double-diffusion instability length scale can be expressed as

$$d = \left( \frac{k_T \nu}{g \alpha_T \frac{\partial T}{\partial z}} \right)^{1/4}, \quad (2)$$

where  $k_T$  is the thermal diffusivity. In lakes and oceans  $d$  is typically 1 cm, and the observed step sizes associated with diffusive layering in these environments (1–10 m) are understood to represent a later evolutionary development of the primary instability. From our data we approximate  $\frac{\partial T}{\partial z} \approx \frac{\Delta T}{\Delta z} \approx \frac{6 \text{ C}}{10 \text{ cm}}$ , which yields  $d = 1$  mm.

Our observed 2 cm steps may likewise represent a larger-scale evolutionary development via merger events. In light of recent theory [18], simulations at  $Ri = 10$  showed the appearance of steps at a nondimensional time of 500, and significant mergers some 1000 time units later. For our shear time scale ( $\leq 6$  s) this translates to real times of about  $3 \times 10^3$  and  $9 \times 10^3$  s, respectively. At lower  $Ri$ , such as ours, even earlier larger-scale development may be expected, so that the times seen in Fig. 8 appear reasonable for this process. From [18] we may also estimate the largest expected scale to be  $h^* = 20H_s \sqrt{Ri}$ , where  $H_s$  is the shear scale height. For our conditions we find  $h^*$  to be a few meters, so 2 cm steps can indeed be considered to be an intermediate scale.

However, given that the step size does not appear to change significantly over the observed time period, another explanation should be considered. The observed step size might instead be the immediate result of a turbulent diffusivity. For instance, step sizes of about 2 cm are obtained when using Eq. (2) with eddy diffusivities  $k \sim U_{\text{rms}} L_{\text{rms}} = 10^{-4} \text{ m}^2/\text{s}$  for both  $k_T$  and  $\nu$ . Whatever the role of background turbulence, we are apparently below the rms level where thermohaline staircases cannot form [28]. We note also that rotational effects have not been taken into account.

Considering previous laboratory experiments, another parameter that might be compared is the thickness of the bottom layer at the time of additional step formation. Most theories, however, do not account for lateral effects, which are surely important here. An exception is the modified

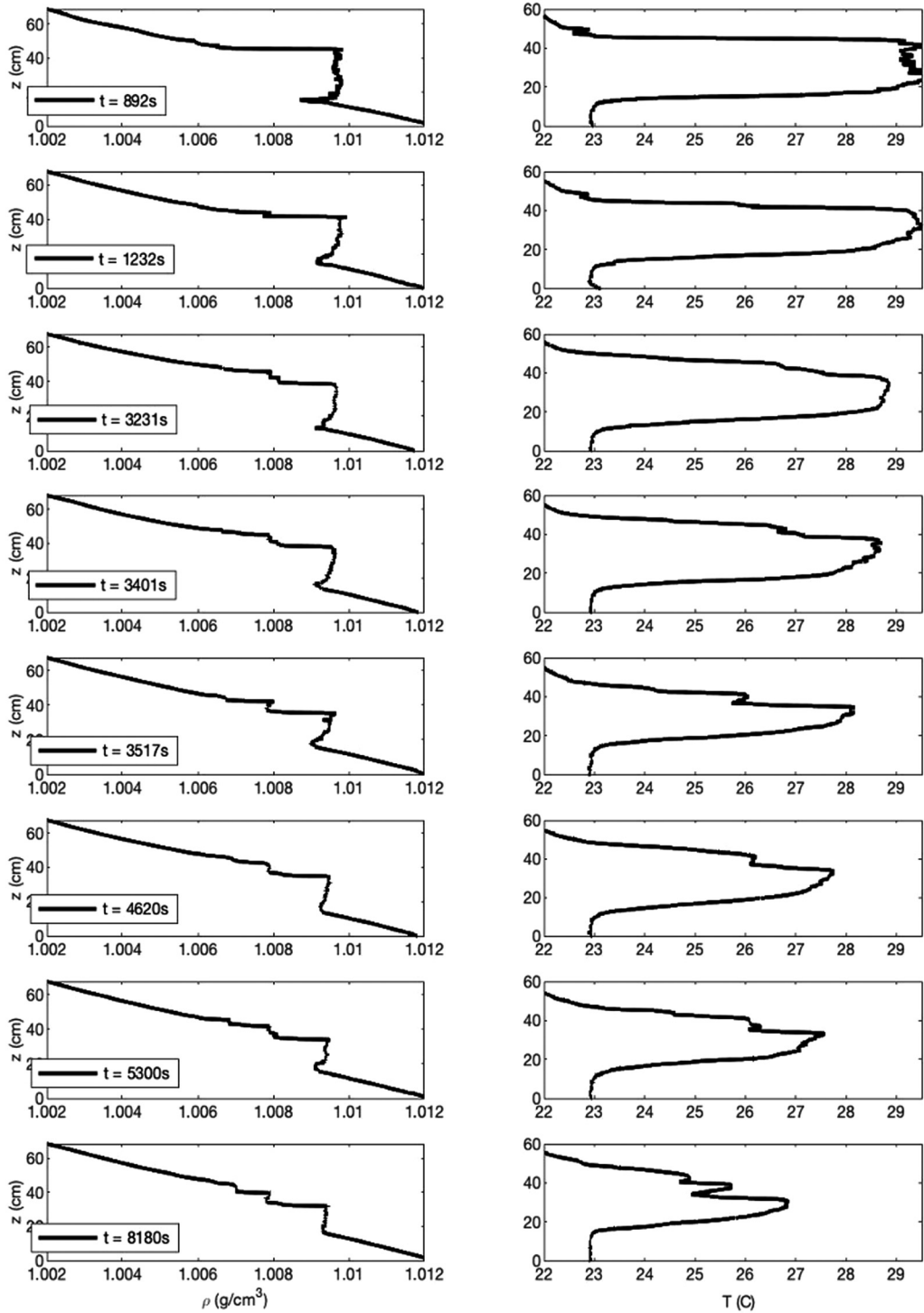


FIG. 8. Probe trace detail showing temporal development of the heated profiles.

intrusion mechanism proposed by Merryfield [29]. Although not as pronounced as the initial period of lateral convection [Fig. 4(a)], the developing profiles of Fig. 8 are suggestive of an intrusive mechanism. In any case, this is one more issue that a more thorough spatiotemporal data set might address.

#### IV. SUMMARY AND OUTLOOK

In summary, we have observed the evolution of large anticyclonic vortices within a rotating, stratified background. An  $m = 2$  baroclinic (or baroclinic-shear) instability quickly develops, leading to subvortices and fine-structured shed filaments. When heated with respect to their surroundings the vortices are subject to two additional instabilities. Prominent early are lateral intrusions leading to 3–5 cm cusplike features due to thermal convection. Much later ( $t \gg T$ ) a couple 2 cm steps develop above the lens due to diffusive convection: the presumed beginnings of a thermohaline staircase. We see no evidence of layering in the nonheated cases, indicating that the process of viscohaline diffusive layering is likely hampered by preexisting turbulence. The turbulent background does not prevent thermohaline layering, however.

Future experimental campaigns should aim to probe the vortices with additional spatiotemporal resolution. This will help determine what effects are localized to the vortex edge and thus more related to intrusions (the intrusion angle being paramount [22]). To obtain better resolution in density and temperature alternate techniques warrant consideration in order to mitigate the perturbative nature of multiple plunging probes. As with earlier experiments [6,12,13] shadowgraph techniques may be employed to highlight step structure. Resolving the evolving flow field within and around each vortex, for example with high resolution 3D-PIV, is ultimately desirable.

In general, systematic changes within a larger data set are needed: e.g., by varying the lens volumes, temperature differentials, and levels of background rotation and stratification. A wider exploratory range of  $N/f$  and  $\alpha$  may thereby be pursued, as in earlier studies [8,10,26,27]. Concerning the aspect ratio, we note in passing that our typical value of  $\alpha = 0.2$  compares well to recent theory [30] (assuming that there is no stratification internal to the vortex), but unfortunately we cannot comment on its long-term development. Given that the vortex formation process—interesting in itself—begins as soon as the influx enters the rotating frame of reference, the influx delivery rate may also be a variable of interest, especially as this determines preexisting turbulence levels.

It is noteworthy that our typical Burger number lies in the optimal range given by [27],  $0.1 < \text{Bu} < 0.4$ , where the baroclinic instability is strongest as measured by the production of subdeformation radius energy. This range of Bu corresponds to mesoscale lenses such as Meddies as well. Whether this is a natural property of all unstable zero-vorticity intrusions observed in the laboratory seems to be a congruous question.

A central area to address going forward is the layer formation process. Is the observed step size the result of turbulent diffusivities, and/or some intermediate scale development? Furthermore, how are these scales and their associated fluxes affected by rotation? As noted above, DDC laboratory experiments to date have not employed rotation, and vortex experiments to date have not explored the effects of internal heating. Strong rotation has recently been shown to significantly affect DDC transport [31], and while this regime may not be pertinent to geophysical flows, it may play a significant role within some stars and larger planets [32].

The role of DDC with regard to geophysical thermal eddies such as Meddies may be of more direct import. Do staircase structures resulting from diffusive convection contribute to thermohaline vortex decay, and ultimately lens lifetime? Though the extrapolation is not insignificant, future experiments may be able to infer some elements of such mesoscale dynamics, and thus contribute to the understanding of a significant oceanic transport mechanism. In any case, since double-diffusive layering in nature is usually found in a mature state of development, further work on diffusive staircase formation processes, considering the issues above, is likely to be revealing.

## ACKNOWLEDGMENT

This project was funded by the Agence Nationale de la Recherche, Grant No. ANR-AAP-SIMI5-6, OLA (Ocean LAYering).

- 
- [1] W. Thomson, Vibrations of a columnar vortex, *Philos. Mag.* **10**, 155 (1880).
  - [2] D. G. Dritschel, The repeated filamentation of two-dimensional vorticity interfaces, *J. Fluid Mech.* **194**, 511 (1988).
  - [3] R. C. Kloosterziel and G. J. F. van Heijst, An experimental study of unstable barotropic vortices in a rotating fluid, *J. Fluid Mech.* **223**, 1 (1991).
  - [4] E. J. Hopfinger and G. J. F. van Heijst, Vortices in rotating fluids, *Annu. Rev. Fluid Mech.* **25**, 241 (1993).
  - [5] P. M. Saunders, The instability of a baroclinic vortex, *J. Phys. Ocean.* **3**, 61 (1973).
  - [6] R. W. Griffiths and P. F. Linden, The stability of vortices in a rotating, stratified fluid, *J. Fluid Mech.* **105**, 283 (1981).
  - [7] E. Thivolle-Cazat, J. Sommeria, and M. Galmiche, Baroclinic instability of two-layer vortices in laboratory experiments, *J. Fluid Mech.* **544**, 69 (2005).
  - [8] K. Hedstrom and L. Armi, An experimental study of homogenous lenses in a stratified rotating fluid, *J. Fluid Mech.* **191**, 535 (1988).
  - [9] A. E. Gill, Homogeneous intrusions in a rotating stratified fluid, *J. Fluid Mech.* **103**, 275 (1981).
  - [10] G. Facchini and M. Le Bars, On the lifetime of a pancake anticyclone in a rotating stratified flow, *J. Fluid Mech.* **804**, 688 (2016).
  - [11] M. E. McIntyre, Diffusive destabilisation of the baroclinic circular vortex, *Geophys. Fluid Dyn.* **1**, 19 (1970).
  - [12] D. J. Baker, Density gradients in a rotating stratified fluid: experimental evidence for a new instability, *Science* **172**, 1029 (1971).
  - [13] J. Calman, Experiments on high Richardson number instability of a rotating stratified shear flow, *Dyn. Atmos. Oceans* **1**, 277 (1977).
  - [14] H. Stommel, A. B. Arons, and D. Blanchard, An oceanographic curiosity: the perpetual salt fountain, *Deep-Sea Res.* **3**, 152 (1953).
  - [15] T. Radko, *Double-Diffusive Convection* (Cambridge University Press, Cambridge, UK, 2013).
  - [16] D. E. Kelly, H. J. S. Fernando, A. E. Gargett, J. Tanny, and E. Ozsoy, The diffusive regime of double-diffusive convection, *Prog. Ocean.* **56**, 461 (2003).
  - [17] J. Turner, The coupled turbulent transports of salt and heat across a sharp density interface, *Int. J. Heat Mass Transfer* **8**, 759 (1965).
  - [18] T. Radko, Thermohaline layering in dynamically and diffusively stable shear flows, *J. Fluid Mech.* **805**, 147 (2016).
  - [19] L. Armi, D. Hebert, N. Oakey, J. Price, P. L. Richardson, T. Rossby, and B. Ruddick, Two years in the life of a Mediterranean salt lens, *J. Phys. Ocean.* **19**, 354 (1989); K. Schultz Tokos, and T. Rossby, Kinematics and dynamics of a Mediterranean salt lens, *ibid.* **21**, 879 (1991).
  - [20] C. Papenberg, D. Klaeschen, G. Krahnmann, and R. W. Hobbs, Ocean temperature and salinity inverted from combined hydrographic and seismic data, *Geophys. Res. Lett.* **37**, L04601 (2010); B. L. Hua, C. Ménésguen, S. Le Gentil, R. Schopp, B. Marsset, and H. Aiki, Layering and turbulence surrounding an anticyclonic vortex: in situ observations and quasi-geostrophic numerical simulations, *J. Fluid Mech.* **731**, 418 (2013); T. Meunier, C. Ménésguen, R. Schopp, and S. Le Gentil, Tracer stirring around a meddy: the formation of layering, *J. Phys. Ocean.* **45**, 407 (2015).
  - [21] H. Song, L. M. Pinheiro, B. Ruddick, and F. C. Teixeira, Meddy, spiral arms, and mixing mechanisms viewed by seismic imaging in the Tagus Abyssal Plain (SW Iberia), *J. Marine Res.* **69**, 827 (2011).
  - [22] B. Ruddick, Intrusive mixing in a Mediterranean salt lens – intrusion slopes and dynamical mechanisms, *J. Phys. Ocean.* **22**, 1274 (1992).

- [23] T. Radko and C. Sisti, Life and demise of intrathermocline mesoscale vortices, *J. Phys. Ocean.* **47**, 3087 (2017).
- [24] <http://www.legi.grenoble-inp.fr/web/spip.php?article757>.
- [25] O. Praud, A. M. Fincham, and J. Sommeria, Decaying grid turbulence in a strongly stratified fluid, *J. Fluid Mech.* **522**, 1 (2005).
- [26] E. Yim, P. Billant, and C. Ménesguen, Stability of an isolated pancake vortex in continuously stratified-rotating fluids, *J. Fluid Mech.* **801**, 508 (2016).
- [27] B. A. Storer, F. J. Poulin, and C. Ménesguen, The dynamics of quasigeostrophic lens-shaped vortices, *J. Phys. Ocean.* **48**, 937 (2018).
- [28] N. C. Shibley and M.-L. Timmermans, The formation of double-diffusive layers in a weakly turbulent environment, *JGR Oceans* **124**, 1445 (2019).
- [29] W. J. Merryfield, Origin of thermohaline staircases, *J. Phys. Ocean.* **30**, 1046 (2000).
- [30] P. Hassanzadeh, P. S. Marcus, and P. Le Gal, The universal aspect ratio of vortices in rotating stratified flows: theory and simulation, *J. Fluid Mech.* **706**, 46 (2012); O. Aubert, M. Le Bars, P. Le Gal, and P. S. Marcus, The universal aspect ratio of vortices in rotating stratified flows: experiments and observations, *ibid.* **706**, 34 (2012).
- [31] R. Moll and P. Garaud, The effect of rotation on oscillatory double-diffusive convection (semiconvection), *Astrophys. J.* **834**, 44 (2017).
- [32] P. Garaud, Double-diffusive convection at low Prandtl number, *Annu. Rev. Fluid Mech.* **50**, 275 (2018).